Article

Not peer-reviewed version

HydroSAR: A Cloud-Based Service for the Monitoring of Inundation Events in the Hindu Kush Himalaya

Franz J. Meyer * , Lori A Schultz , Batuhan Osmanoglu , Joseph H Kennedy , MinJeong Jo , Rajesh Bahadur Thapa , Jordan R Bell , Sudip Pradhan , Manish Shrestha , Jacquelyn Smale , Heidi Kristenson , Brooke Kubby , Thomas Joseph Meyer

Posted Date: 24 June 2024

doi: 10.20944/preprints202406.1640.v1

Keywords: SAR; hazard monitoring; cloud computing; Sentinel-1; flooding; Hindu Kush Himalaya

Preprints.org (www.preprints.org) | NOT PEER-REVIEWED | Posted: 24 June 2024 doi:10.20944/preprints202406.1640.v1

Article

HydroSAR: A Cloud-Based Service for the Monitoring of Inundation Events in the Hindu Kush Himalaya

Franz J. Meyer [1,2,†], Lori A. Schultz [3,†], Batuhan Osmanoglu [4,†], Joseph H. Kennedy [2,†], MinJeong Jo [4,†], Rajesh B. Thapa [5,†], Jordan R. Bell [3], Sudip Pradhan [5], Manish Shrestha [5], Jacquelyn Smale [2], Heidi Kristenson [2], Brooke Kubby [1], and Thomas Meyer [1]

[1] Geophysical Institute, University of Alaska Fairbanks, Fairbanks, Alaska, 99775, USA; fjmeyer@alaska.edu
[2] Alaska Satellite Facility, University of Alaska Fairbanks, Fairbanks, Alaska, 99775, USA
[3] NASA Marshall Space Flight Center, Huntsville, Alabama, USA
[4] NASA Goddard Space Flight Center, 8800 Greenbelt Rd, Greenbelt, Maryland, 20771, USA
[5] International Centre for Integrated Mountain Development, G.P.O. Box 3226, Kathmandu, Lalitpur, 44700, Nepal
* Correspondence: fjmeyer@alaska.edu; Tel.: +49-907-474-7767
† These authors contributed equally to this work.

Abstract: The Hindu Kush Himalaya (HKH) is one of the most flood-prone regions in the world, yet heavy cloud cover and limited in-situ observations have hampered efforts to monitor the impact of heavy rainfall, flooding, and inundation during severe weather events. This paper introduces HydroSAR, a Sentinel-1 SAR-based hazard monitoring service that was co-developed with in-region partners to provide year-round, low-latency weather-hazards information across the HKH. The paper describes the end-user focused concept and overall design of the HydroSAR service. It introduces the main processing algorithms behind HydroSAR's broad product portfolio, which includes qualitative visual layers as well as quantitative products measuring surface water extent and water depth. We summarize the cloud-based implementation of the developed service, which is providing capability to scale automatically with event size. A performance assessment of our quantitative algorithms is described, demonstrating capabilities to map flood extent and water depth at an accuracy of >90% and <1m, respectively. An application of the HydroSAR service to the 2023 South Asia monsoon seasons shows that monsoon floods peaked around August 6, 2023 and covered 11.6% of Bangladesh in water. At the peak of the flood season, nearly 13.5% of Bangladesh's agriculture areas were affected.

Keywords: SAR; hazard monitoring; cloud computing; Sentinel-1; flooding; Hindu Kush Himalaya

---

1. Introduction

Floods are considered the most significant natural disaster affecting the low-lying floodplains of the Hindu Kush Himalaya (HKH) from the perspective of their frequency, financial cost, and impact on population and socio-economic activities [1]. For example, the 2019 monsoon season affected 7.3 million people, caused 119 fatalities, and displaced an estimated 308,000 people in Bangladesh alone. The same event additionally caused floods and landslides across Nepal and displaced more than 1.8 million people in the northern reaches of India [2].

A review of past studies of flooding events in the HKH, published in [3], concluded that floods in the region cannot be completely controlled and that efforts should be directed towards reducing flood vulnerability and mitigating impacts through improved flood risk management. To accomplish efficient and effective flood risk management, near real-time information on inundation extent, water depth, and impacts on agriculture are necessary to guide appropriate disaster risk reduction activities [4].

Regularly acquired, weather-independent synthetic aperture radar (SAR) observations such as those from ESA's Sentinel-1 [5] and the upcoming NASA-ISRO SAR (NISAR) [6] missions have the potential to meet this critical data need. Previous case studies have identified SAR as a useful data set for mapping floods and other weather-related hazards [7–11], yet, novel data processing approaches were still needed to cope with the large data volumes associated with SAR and enable the automatic generation of hazard information at low latency and across large spatial scales.

The increasing availability and reduced latency of SAR observations has generated growing interest in the development of such automatic flood monitoring algorithms. The German Aerospace Center's (DLR) Center for Satellite based Crisis Information (ZKI) developed a thresholding algorithm to monitor flood water extent from Sentinel-1 and TerraSAR-X SAR data [7,12]. Similar thresholding techniques were also developed by a variety of other teams [4,13,14] to provide flood extent information for individual events in China, Bangladesh, and the Mekong delta. A recent work published in [15] developed an automatic system for flood extent and flood duration mapping using multi-sensor satellite observations. This system is based on four processing chains for the derivation of flood extent from Sentinel-1 and TerraSAR-X radar as well as from optical Sentinel-2 and Landsat satellite data.

Despite these advances, current services are often characterized by a rather narrow product portfolio (e.g., surface water extent only), providing only limited information about an ongoing event. Furthermore, most existing systems lack a scalable computing architecture, limiting their ability to continue to provide low-latency information as the size of an event increases. Lastly, many current efforts did not emphasize co-development and transitioning of developed technology to an in-region partner when defining product portfolios, processing solutions, and delivery mechanisms of their services. This may limit the impact of their work on decision-making practices in a specific target region.

In this paper, we introduce HydroSAR, a cloud-based SAR data analysis service that was co-developed with end-user partners for the monitoring of hydrometeorological events in the Hindu Kush Himalaya. Funded through a NASA SERVIR Applied Science Team grant, HydroSAR includes a series of SAR-based value-added products for the monitoring of surface hydrology (image time series, flood extent, water depth, and affected agriculture) in the region. Product algorithms were selected, adapted and operationalized based on a review of recent literature and in collaboration with end-user partners in the flood-prone Hindu Kush Himalaya region. The goal of HydroSAR was to develop a more complete set of hazard data layers than most comparable systems, enabling the simultaneous assessment of surface water extent, water depth, and flood impacts on agriculture.

After motivating our work with a summary of flood mapping needs in the HKH (Section 2), we discuss our co-development strategy that was implemented to ensure that HydroSAR meets the needs of end-users in the region (Section 3). The selected HydroSAR product portfolio and product algorithms are summarized in Section 4. Section 5 introduces the cloud-based implementation of HydroSAR, providing the capability to scale automatically with event size and enabling near real-time access production of actionable information even for events of very large spatial scales. After presenting our visualization and data sharing concepts in Section 6, Section 7 provides a performance assessment of HydroSAR product algorithms by comparing SAR-derived products to reference information provided by in-region partners or derived from different sensors. Finally, we demonstrate the impact of our service by applying HydroSAR products to the 2023 monsoon season (Section 8). A summary and outlook conclude the paper.

2. Flood Mapping Needs in the HKH

The HKH region extends over 3500 km, encompassing Myanmar in the East and reaching to Afghanistan in the West (dark blue region in Figure 1). With its high variability of topography, the region hosts ten large rivers including Mekong, Yangtse, Yellow River, Salween, Irrawady, Brahmaputra, Ganges, Tarim Indus, and Amu Darya, making large areas of Afghanistan, Bangladesh, India, Nepal, and Pakistan susceptible to inundation by floodwaters during every rainy season [2]. Among these countries, Bangladesh has been experiencing record-high floods occurring almost every year due to Bangladesh's unique geographical setting as the most downstream country in the HKH [16]. On average, about $26,000 km^2$ of Bangladesh is inundated every year during the peak of the monsoon season [1]. Floods can persist for several weeks in some regions of the country.

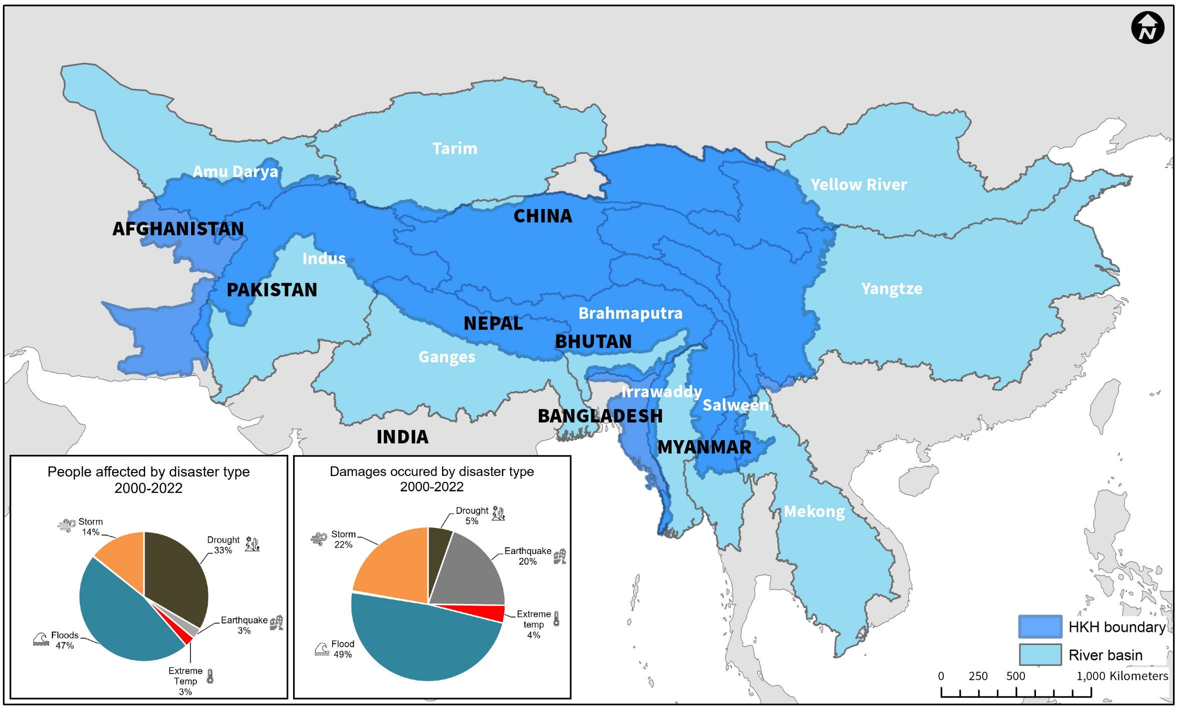

Figure 1. Survey of disaster impacts in the HKH using data from the international disaster database EM-DAT (https://www.emdat.be/). The data show that flooding events are the predominant hazard affecting communities in the region, resulting in the majority of economic damages.

Rapid change during the recent global warming period has altered meteorological and hydrological extreme events in the HKH, giving rise to a further increase in the frequency of flood hazards [2,8]. Today, large areas of Bangladesh, Bhutan, India, Nepal, and Pakistan are subject to frequent extreme weather events, creating a hazard environment where floods can damage infrastructure, and threaten livelihoods.

Climate change-enhanced variability of precipitation patterns and associated increases in the occurrence of floods have also affected agricultural productivity and income across the HKH region and have led to increased vulnerability and uncertainty in food and nutrition security [17]. A survey of disaster impacts between 2000 and 2022 shows that floods have become the most common hazard in the HKH [3], accounting for 47% of people affected and 49% of the annual economic loss caused in the region (Figure 1).

A key element of weather- and climate-related disaster risk reduction (DRR) is near real-time access to actionable information on surface water extent, water depth, and event impacts on settlements and agriculture [18]. Unfortunately, the HKH region lacks in-situ observations for monitoring the impact of heavy rainfall, flooding, and inundation during severe weather events due to both the remoteness of the region as well as limited technical and economic capacity.

3. Co-Developing an Inundation Monitoring Service for the HKH

As for any SERVIR-funded service, co-development and transitioning of developed technology to an in-region partner organization was a central part of the HydroSAR service development cycle. To ensure the HydroSAR service is sustainable and meets end-user needs, we utilized a SERVIR-pioneered co-development process, where end-user agencies and the HydroSAR project team jointly agreed on project specifications and created a method to monitor the impact of the service, with a monitoring, evaluation, and learning (MEL) approach [19]. As displayed in Figure 2 our service development approach used a systematic process of designing and integrating user needs and preferences throughout the service development process until eventual service delivery. This process was intended to ensure that the HydroSAR effort remains responsive, effective, and needs driven [19].

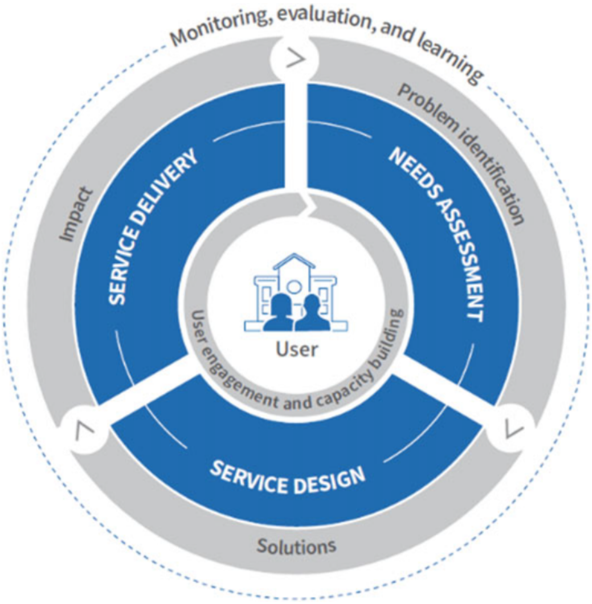

Figure 2. NASA SERVIR co-development process used in HydroSAR service development to ensure that HydroSAR is sustainable and meets end-user needs.

In this process, we worked most closely with the International Centre for Integrated Mountain Development (ICIMOD), an intergovernmental knowledge and learning center that develops and shares research with the eight regional member countries of the HKH – Afghanistan, Bangladesh, Bhutan, China, India, Myanmar, Nepal, and Pakistan [20].

As one of the core member organizations of the project, and as the hub of SERVIR in the Hindu Kush Himalaya, ICIMOD (https://servir.icimod.org/) facilitated end-user consultations, training activities with partner countries, in-situ data collections, and field verifications throughout the project development phase. Jointly with ICIMOD, we conducted several consultation meetings and training activities, inviting relevant stakeholders working on flood management practices. The participants of the workshops were comprised of government and non-government agencies from Bangladesh, Bhutan, and Nepal. Stakeholder feedback collected during these consultation meetings and capacity building events were used to refine product specification and delivery mechanisms of the HydroSAR service.

ICIMOD is now the host of the completed and operational HydroSAR service and is continuing to evaluate the impact of HydroSAR technology through existing partnership arrangements with national agencies in the HKH region.

4. HydroSAR Product Portfolio and Product Algorithms

Based on the information in Section 2, developing a SAR-based weather-hazards monitoring system capable of providing low-latency flood impact information on a regional scale and during all weather conditions was a necessity [21] for the HKH region [4].

Therefore, in collaboration with end-user partners of ICIMOD, we designed the HydroSAR service to provide near real-time access to a comprehensive set of SAR-derived information products to allow assessment of surface water extent, water depth, and flood impacts on agriculture. Our coordinated set of hazard information products along with their data dependencies is shown in Figure 3. The product portfolio combines visual aids to be used by analysts with quantitative products on flood status and flood impact.

All HydroSAR products are generated in cloud-optimized GeoTIFF (CoG) format so that data can be efficiently accessed and distributed in the cloud (Section 5). They are presented to analysts and other end-users through a dedicated web portal discussed in Section 6.

The purpose and implementation of each individual product is described in the following subsections. For the purpose of brevity, we will focus on the visual aids (RTC30; RTC30-Color) and quantitative flood-water products (HYDRO30; WD30) in this paper, for which automatic processing workflows are implemented. While HydroSAR also includes an agriculture extent product (AG30), this product is not yet included in the HydroSAR web portal and will not be discussed here. Readers interested in the concepts behind AG30 are referred to [22] for more information.

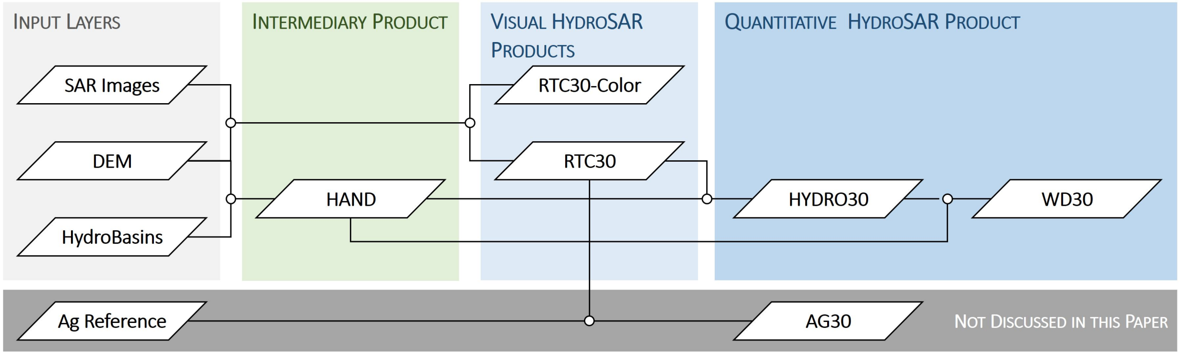

Figure 3. Portfolio of flood hazard products created by HydroSAR to support the analysis of flood status and impact. Input data are shown on the left. The green column shows intermediary products needed to generate the final visual and quantitative HydroSAR products shown on the right side of the figure. Lines indicate workflows and dataset dependencies The HydroSAR agriculture extent product AG30 is not discussed in this paper but is included for completeness.

4.1. Input Data

Input data for HydroSAR are shown in Figure 3 and consist of SAR data, digital elevation model (DEM) information, as well as ancillary information such as hydrobasins and agriculture reference data. Data used for product validation are presented in Section 7.

SAR data used in HydroSAR consists of NASA-managed Sentinel-1 SAR data holdings at the NASA Alaska Satellite Facility (ASF) Distributed Active Archive Center (DAAC). The Sentinel-1 C-band SAR constellation has been providing free-and-open, globally-observed SAR data since 2014 and is observing all global land masses at high sampling rates. Sentinel-1 provides complete coverage of the HKH once every 8-10 days. Data are typically processed and delivered to the ASF DAAC within 6 hours after image acquisition. With its global acquisition strategy, its cloud-free imaging capabilities, and its comparably low latency data delivery, Sentinel-1 provides an excellent basis for HydroSAR's inundation mapping goals.

DEM data used in this project consist of the 30-m resolution Copernicus GLO-30 Digital Elevation Model [23]. This freely-accessible resource is based on acquisitions of the TanDEM-X mission, a constellation of two satellites flown with the goal to generate a global DEM [24]. GLO-30 is a validated DEM [25] and provides consistent-quality topographic information across our area of interest. The HydroSAR processor accesses the COP-DEM directly in AWS through its Registry of Open Data program.

Beyond these data types, We use ancillary information about watersheds and land cover in some of our processing routines (see Section 4.2.1). Hydrobasin information is accessed from the HydroSHEDS database [26], which offers a suite of global digital data layers in support of hydro-ecological research and applications worldwide. Landcover information used in HydroSAR originates from the Copernicus Global Land Monitoring Service [27].

4.2. *Intermediary Data Products and Visual Aids*

4.2.1. Height Above Nearest Drainage

Hand is a terrain descriptor calculated from a hydrologically coherent DEM [28]. The HAND model normalizes topography based on local relative heights observed along a drainage network (Figure 4). In the HAND grid, each pixel value indicates the vertical distance between a specific location and its nearest drainage stream. HAND can be calculated for individual hydrological basins such as HydroSHEDS [26] under the assumption that each basin is self-contained. HAND can also be calculated independent of hydrological basin information, in a tiled approach when calculating it over large regions. In this case, a buffer is used to eliminate any edge effects due to tiling.

Regardless of the domain, HAND calculation is done the same way. First, the provided input DEM is conditioned to be hydrologically correct. This is achieved by filling in depressions, where a cell region has much lower value than their surrounding neighbors. We then resolve the flat areas to identify drainage basins. With drainage basins at hand, flow directions can be calculated allowing for the generation of routing patterns, which are used to calculate the total accumulations showing the number of pixels draining into another. At the final step, these accumulation values are used to calculate HAND using an accumulation threshold and eight-directional flow, also known as D8. The accumulation threshold determines the drainage mask based on the total accumulation for a given cell, directly impacting the output. Figure 4 illustrates the relationship between the source DEM and the HAND product. Upon comparing the heights in Figure 4(c), it becomes evident that the slope and trend of the DEM have been removed from the HAND product. The accumulation threshold can adjust the strength of this impact. In this study we used an accumulation threshold of 100 pixels, and calculated HAND without splitting the DEM based on basins [29].

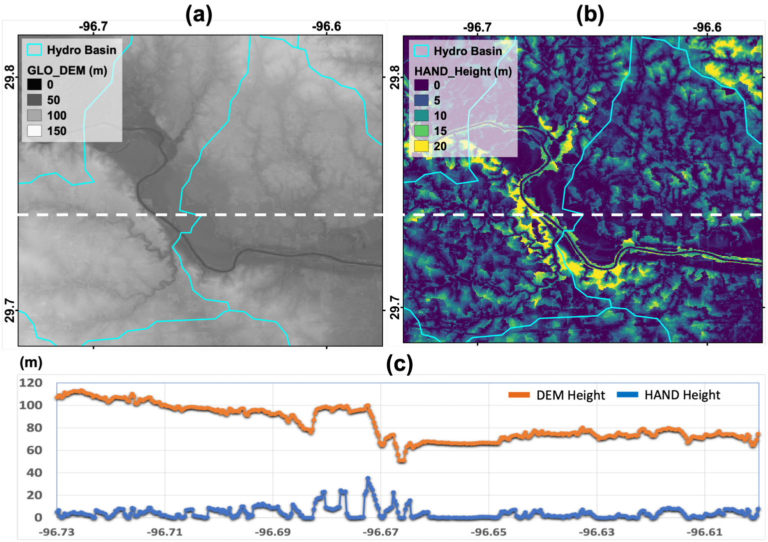

Figure 4. An example of topographic heights and the HAND model: (a) Copernicus 30-m DEM; (b) HAND model height generated from the DEM; (c) Heights comparison between the source DEM and the HAND model

4.2.2. RTC30 Product

Previous research has demonstrated the benefits of Radiometric Terrain Correction (RTC) processing for many mapping and hazard monitoring applications [10,11,30,31]. The removal of topography-induced radiometric biases (topographic shading) from SAR images aids in the visual interpretation of SAR amplitude data by analysts. Furthermore, RTC processing reduces the requirement for exact repeat acquisitions in change detection algorithms by mitigating differences between images that are introduced by changes in observation geometries [10].

Based on end-user input, HydroSAR's RTC30 product (Figure 5a) was designed as a 30-m RTC-processed SAR image product and serves as a visual aid and as an essential base data set in the HydroSAR service. RTC30 forms the basis for most higher-level data products in the HydroSAR product portfolio (Figure 3).

We utilize the pixel-area integration approach proposed by Small [32] to perform RTC processing. In this approach, radiometric normalization is done by determining the actual area on the ground for every SAR resolution cell. According to [10], the average normalized backscatter coefficient, σ^0, for a pixel is calculated via

$$\sigma^0 = \beta^0 \cdot \frac{A_{\sigma^0_{cos}}}{A_{\sigma^0_{pa}}} \quad [dB] \tag{1}$$

with the (calibrated) radar brightness β^0, the ellipsoid reference area $A_{\sigma^0_{cos}}$, and the illuminated topographic pixel area $A_{\sigma^0_{pa}}$ [33]. In our algorithm, the σ^0 data from Equation (1) are further projected into the γ^0 space using the local incidence angle θ:

$$\gamma^0 = \frac{\sigma^0}{cos(\theta)} \quad [dB] \tag{2}$$

For land applications, γ^0 provides the best measure for image classification and time series analysis [33]. Single Look Complex (SLC) Sentinel-1 Interferometric Wide Swath (IW) data along with the 30-m resolution Copernicus GLO-30 DEM are used to generate the HydroSAR RTC30 products. For ease of integration into our cloud-based workflows, RTC-30 data are generated as cloud-optimized GeoTIFFs. For more information on the RTC algorithm implementation see [29]. For information on the performance of the underlying RTC algorithm, please see [32].

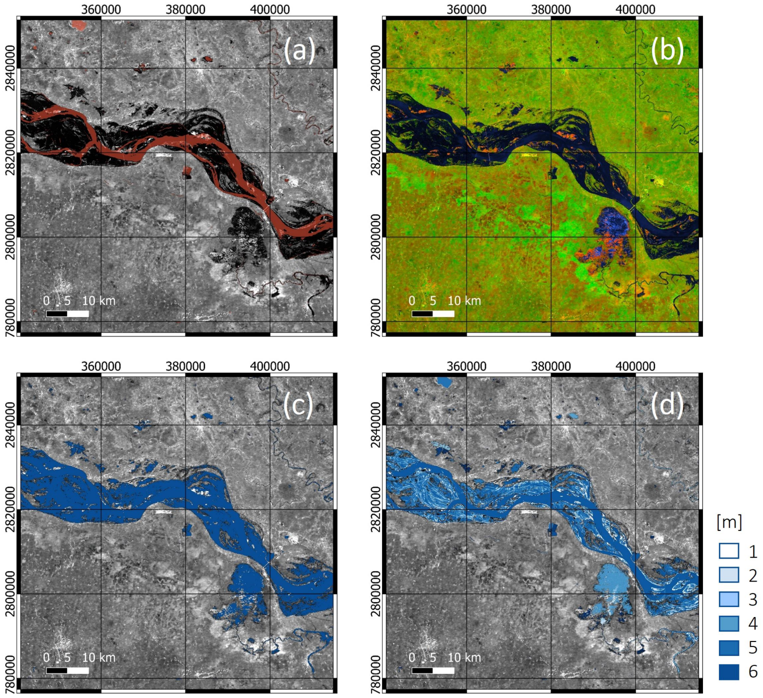

Figure 5. Example of HydroSAR flood-relevant data products for an area around the Ganges River, Bihar, India: (a) RTC30 product. Red shaded regions correspond to the permanent water extent in this region; (b) RTC30-Color image with surface water showing in dark blue colors; (c) HYDRO30 surface water extent product on top of an RTC30 image; (d) WD30 water depth product on top of RTC30.

4.2.3. RTC30-Color

To ease the uptake of SAR data by end-user organizations in the HKH, the HydroSAR team was asked to develop a product that is easy to interpret by analysts mostly familiar with optical data. In response to this request, we developed a simplified polarimetric decomposition concept that is based on dual-pol Sentinel-1 RTC-30 data and results in RGB-formatted image products that approximate the look-and-feel of visual-band data.

The approach decomposes the co- and cross-pol signal into simple bounce (polarized) with some volume scattering, volume (depolarized) scattering, and simple bounce with very low volume scattering components. These are assigned to the red, green, and blue color channels of an RGB composite according to:

$$\begin{aligned} R &= a(VV - 3HV)^{0}.5 \quad && \text{when } HV > k \\ G &= b(HV)^{0}.5 && \\ B &= c(VV)^{0}.5 && \text{when } HV \leq k \end{aligned} \tag{3}$$

where a, b, and c are empirically determined to create a histogram-balanced image, and k is set near the image noise floor. In the case where the volume to simple scattering ratio is larger than expected for typical vegetation, such as in glaciated areas or some forest types, a teal color (green + blue) is used.

The convenience of the RGB decomposition in Equation 3 for monitoring surface water extent stems from the fact that the blue channel is predominately associated with surface water, providing an easy-to-understand visual aid for response personnel. Figure 5b shows an RGB composite product for an area around the Ganges River, Bihar, India. In this example, water areas can be identified in blue, while vegetated areas show in shades of green and urban environments appear in red and orange hues.

4.3. Quantitative HydroSAR Flood Information Products

4.3.1. HYDRO30: Surface Water Extent

Our 30-m surface water extent product, HYDRO30, is a modified version of an algorithm published in [34] and performs adaptive thresholding of dual-pol RTC30 images to derive surface water extent. A HAND layer, derived from the Copernicus GLO-30 DEM, is included to improve robustness. The HYDRO30 algorithm includes the following processing steps, also visualized in Figure 6:

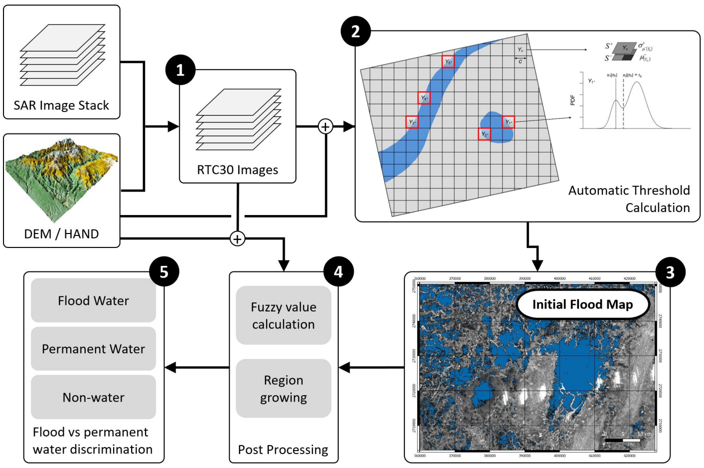

Figure 6. Summary of the HydroSAR HYDRO30 workflow consisting of RTC generation (see Section 4.2.2), threshold calculation, selection of candidate water pixels, a post-processing refinement step, permanent and flood water discrimination and product dissemination.

Preprints.org (www.preprints.org) | NOT PEER-REVIEWED | Posted: 24 June 2024 doi:10.20944/preprints202406.1640.v1

Step 1: Preparing Input Data: We use the algorithms described in Sections 4.2.1 and 4.2.2 to generate HAND and RTC30 product layers needed for surface water threshold calculation. Due to the large data volumes associated with this regional scale monitoring effort, we perform these operations in the cloud-based processing environment (Section 5) that hosts HydroSAR. HAND data and RTC30 products are generated at 30-m resolution and in CoG formats.

Steps 2 & 3: Adaptive Threshold Calculation: We use a modified version of the adaptive thresholding approach in [12] to identify surface water candidate pixels from the RTC30 input data. Like in [12] we utilize a bi-level quadtree tile structure to ensure robust threshold calculation. We first divide the scenes into a parent level structure with a tile size of 100 × 100 pixels. Each parent tile is subsequently sub-divided into 2 × 2 child objects of 50 × 50 pixels each.

Once this structure was created, we use the following three criteria to select the subset of parent tiles most suitable for automatic threshold calculation:

- For each parent tile, we calculate the coefficient of variation (CV) of the mean radar brightness values of its four child objects. This is a departure from [12], who used the standard deviation as a metric. We found CV to be more robust across regions with different average radar brightness. Parent tiles with high CV are potential candidates for threshold calculation as high CV is expected for tiles that contain both water and land semantic classes. Tiles that offer the highest (>95% percentile) CV are selected as candidates.
- We require parent objects to have mean radar brightness lower than the mean of all parent tiles. This ensures that tiles lying on the boundary between water and land areas are selected.
- To improve the robustness of the threshold calculation we exclude parent tiles that are not in flood-prone regions. To do so we label pixels with HAND elevations $\leq 15m$ as unlikely to be flooded. Tiles are only considered if less than 20% of their pixels are identified as not flood prone.

We select the $N = 5$ best tiles for threshold calculation using the CV of the mean radar brightness values as ranking metric. We calculate threshold values for each of these $N = 5$ tiles using expectation maximization [11] and define the best scene-wide classification threshold τ_g as the arithmetic mean of the 5 individual thresholds.

Using this dynamically calculated threshold, both the VV and VH bands of the Sentinel-1 RTC30 data are classified into water and no-water classes and the classification maps derived for VV and VH are combined to create a combined surface water candidates mask.

Step 4: Fuzzy Logic Post Processing: Similar to [34], fuzzy logic post-processing is used to identify and remove false water defections from the surface water candidates mask. Fuzzy rules are established for (i) radar brightness, (ii) HAND elevation, (iii) surface slope, and (iv) water patch size. The rule set is designed to ensure that dark pixels with low HAND elevation and low surface slopes receive higher likelihoods to be true flood pixels [35].

1. **RCS**: $\left\{\begin{array}{lcl} x_{u,RCS} & = & \tau_g \\ x_{l,RCS} & = & \mu_{\sigma^0(\tau_g)} \end{array}\right\}$ with $\sigma^0(\tau_g)$ = RCS of initial flood candidate pixels.
2. **HAND**: $\left\{\begin{array}{lcl} x_{u,HAND} & = & \mu_{HAND(water)} + 3 \cdot \sigma_{HAND(water)} \\ x_{l,HAND} & = & \mu_{HAND(water)} \end{array}\right\}$.
3. **Surface slope** α: $\left\{\begin{array}{lcl} x_{u,\alpha} & = & 0^\circ \\ x_{l,\alpha} & = & 15^\circ \end{array}\right\}$.
4. **Area** A: $\left\{\begin{array}{lcl} x_{u,A} & = & 10px \\ x_{l,A} & = & 3px \end{array}\right\}$.

Our second fuzzy rule deviates from the approach in [34], which uses DEM heights rather than HAND. As a hydrologically-conditioned variable, we found HAND to lead to more hydrologically relevant fuzzy weights and fewer rejections of true water pixels.

Fuzzy membership functions are calculated for each of indicators using Z-shaped activation functions. Membership scores are averaged and a threshold of 0.45 is applied to remove false detections.

doi:10.20944/preprints202406.1640.v1

Step 5: Discrimination of Permanent and Flood Related Water: In a final step, we separate perennial water from flood related surface water using reference data from the Joint Research Centre global surface water dataset. The initial version of this data set was produced using Landsat images at 30-m resolution acquired between 1984 and 2021 [36] and is currently updated annually.

HYDRO30 products are operationally created across the HKH as part of the HydroSAR service. An example of a HYDRO30 product is shown in Figure 5(c) and a performance assessment is presented in Section 7.

4.3.2. WD30: Water Depth

The HydroSAR 30-m water depth product WD30 is computed based on HAND and the HYDRO30 water extent product described in Section 4.3.1. The calculation is done separagely for each independent water patch. Our WD30 workflow is shown in Figure 7a and consists of the following steps:

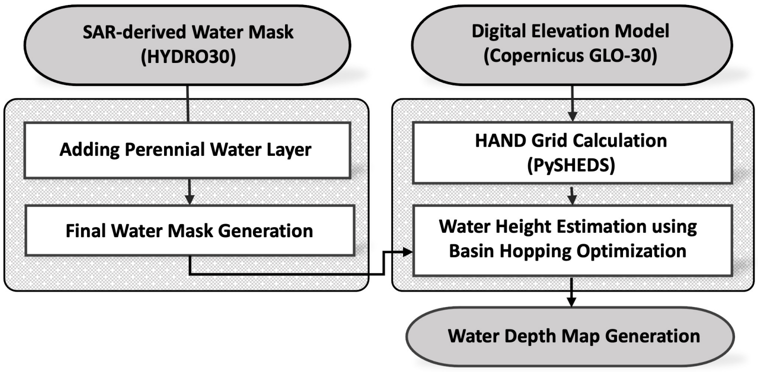

(a)

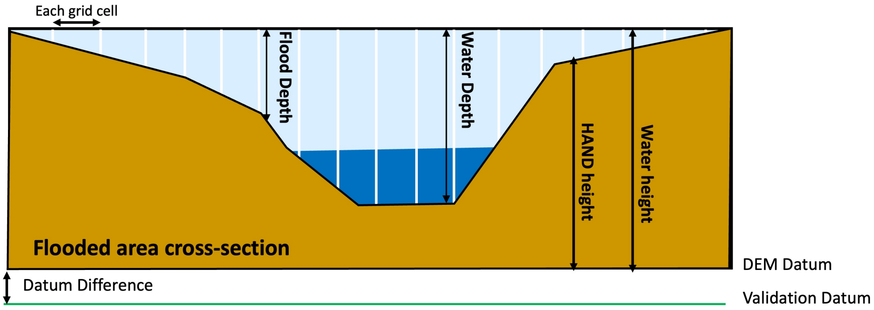

(b)

Figure 7. (a) The workflow of water depth estimation and (b) the cartoon showing the terms used in the workflow.

Step 1: Fetching HYDRO30 and HAND from HydroSAR Cloud Storage: While any GDAL-compatible water extent map can be used to generate a water depth map, the HYDRO30 products are used as fundamental inputs for WD30 calculation. HYDRO30 and the HydroSAR HAND products are fetched from the HydroSAR cloud storage bucket to prepare for water depth derivation.

Step 2: Integrating Water Extent Maps and Perennial Water Layer: We combine the perennial water layer mentioned in Section 4.3.1 with the observed water extent maps to ensure gap-free coverage of perennial water bodies. Gaps in SAR-based water extent maps may occur due to man-made structures such as bridges or dams, or due to overhanging vegetation. The primary role of the perennial water layer is to close potential gaps and connect water bodies that are expected to be connected.

Step 3: Water Height Estimation using Basin-Hopping: Water depths are estimated using the basin hopping algorithm [37], an iterative estimator that identifies the optimal match between the observed water extent and simulated water extent provided by the HAND grid and the maximum water height 7b. The basin hopping algorithm tries to find the best matching surface water extent by flooding HAND at different water levels and comparing the resulting extent with the HYDRO30 product. The search space is bounded to be between 0 and 15m, and the basin-hopping step size is set to 3m. This basin-hopping step size reduces the likelihood of the algorithm converging to a local minimum, which manifests itself as varying results in repeating basin-hopping runs, which by default has a random initial seed. Once the best fitting water height is estimated, water depth is calculated by subtracting HAND from the the estimated water height (Figure 7b). An example of a WD30 product is shown in Figure 5d. A performance assessment of this product is presented in Section 7.

5. HydroSAR Cloud Computing Environment

The presented HydroSAR processing algorithms are implemented in the Amazon Web Services (AWS) cloud (Figure 8) to enable rapid processing across large spatial scales [35]. This cloud approach provides an innovative, open, scalable, and sustainable processing solution for the HKH, ready for continued operation by our in-region partners at ICIMOD. To achieve a cloud architecture that is both performant and cost effective, we partnered with the NASA Alaska Satellite Facility (ASF), who have extensive cloud development expertise from their preparations for the upcoming NASA-ISRO SAR (NISAR) mission.

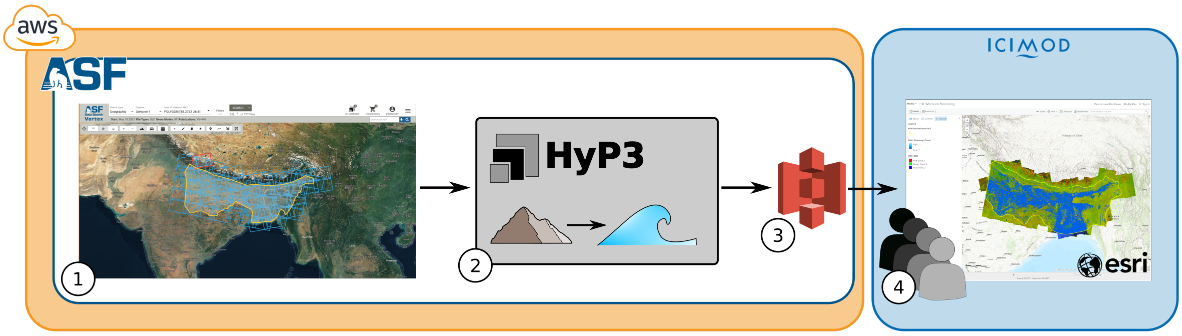

Figure 8. Cloud architecture of the HydroSAR service including (1) integration with ASF's cloud-based archives; (2) HydroSAR product generation in the cloud using ASF HyP3; (3) Temporary product storage in AWS S3; and (4) data delivery to end users via an image service.

As shown in Figure 8, HydroSAR utilizes and seamlessly integrates with two existing ASF-supported services to provide a streamlined user experience: ASF's cloud-based data archive and ASF's Hybrid Pluggable Processing Pipeline (HyP3) [38]. The resulting service is able to produce hundreds to thousands of higher-level products an hour. ArcGIS Image services are used to allow for automatic integration of data products into web portals and for use within desktop GIS environments at HKH partner organizations.

The cloud architecture of HydroSAR includes the following components (Figure 8):

1. **Integration with ASF's cloud-based archives** achieved by co-locating the HydroSAR services with ASF's archives in AWS region us-west-2. This design reduces data movement and enables rapid in-region data access without requiring data download;
2. **Cloud-based HydroSAR product generation** is facilitated by ASF HyP3, a cloud-scaling service allowing to run science algorithms automatically on regional to global scales. Mature HydroSAR workflows are integrated into HyP3 using Docker containers [39] and are run automatically whenever new SAR data over an area of interest hits the ASF archive;
3. **HydroSAR Cloud Storage** is provided in the form of an AWS S3 storage bucket. HydroSAR products are deposited in this bucket immediately after product generation and stored temporarily until pickup by ICIMOD;
4. **Product delivery** to end-users is facilitated by ICIMOD. Using a cron job scheduler utility, ICIMOD fetches new HydroSAR product on a daily basis from the project maintained S3 bucket

for inclusion into their local database. ICIMOD serves out HydroSAR data to its end users via an image service-supported web interface (see Section 6).

The HydroSAR service has been using this implementation to generate flood hazard information across the HKH region and serve these products to end users in Nepal, Bangladesh, Bhutan, and northern India via a dedicated web application that is described in more detail in the following section.

6. Product Visualization and Access Mechanisms

We worked with ICIMOD to co-develop a web portal for the visualization, analysis, and download of HydroSAR data products. The web application is openly available to the general public and has been used by end-users for inundation assessment in the HKH since 2022.

In its role as an intergovernmental organization, ICIMOD has been maintaining a number of science applications that use Earth observation data together with ground-based observations and advanced geospatial information technology to help decision makers respond to environmental hazards in the HKH. To provide consistency across this science applications portfolio, ICIMOD has developed unified service design principles that were also followed when designing the HydroSAR service (Figure 9):

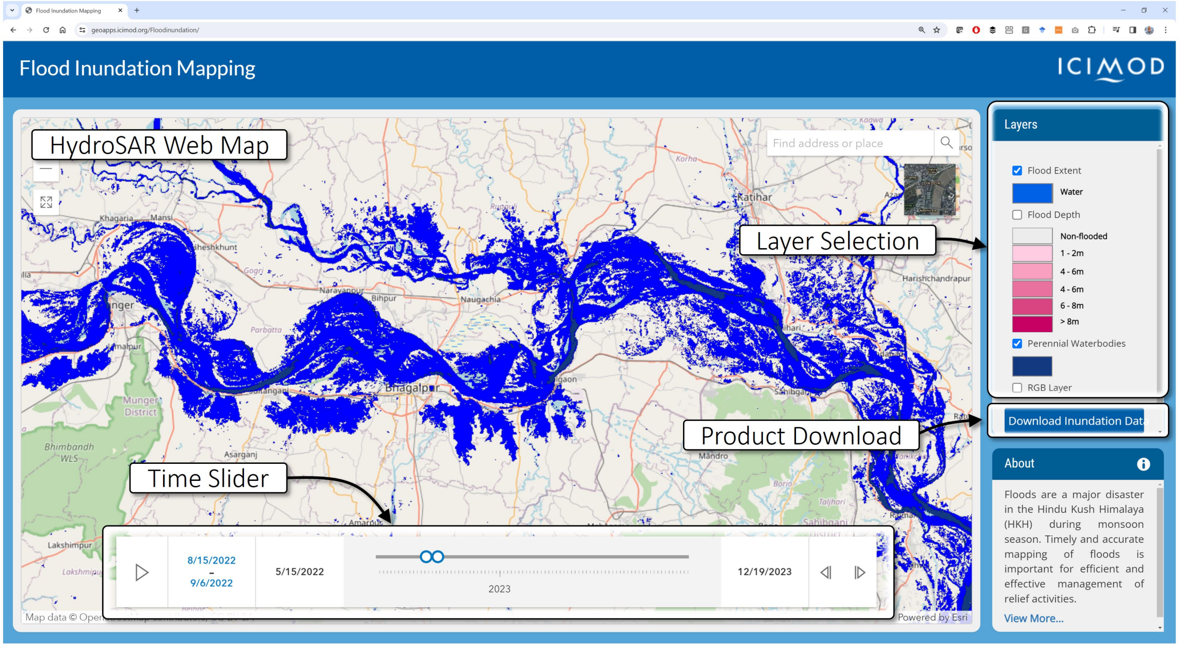

Floods are a major disaster in the Hindu Kush Himalaya (HKH) during monsoon season. Timely and accurate mapping of floods is important for efficient and effective management of relief activities.

View More...

Figure 9. The HydroSAR inundation mapping web application designed and maintained by ICIMOD. The application includes (1) webmap-based visualization of HydroSAR data products, an option to analyze changes in flood parameters with time, and capabilities to access and download individual HydroSAR products.

- Data products are exposed through the public via a web mapping service that allows visualizing water extent and depth information in a geographic context. This web map is supported by an ArcGIS image service in the backend, making it simple to distribute HydroSAR resources to desktop, mobile, and browser applications.
- A time slider is included to support the assessment of changes in water extent and depth over time.
- A layer selector provides the capability to switch between different HydroSAR data products for cross-comparison, cross-validation, and joint hazard assessment.
- A product download feature allows users to access and download HydroSAR products over their area of interest.

Access to and download of HydroSAR data products is facilitated by ICIMOD's Regional Database System (RDS), a one-stop data portal for the HKH. The HydroSAR inundation data download tool shown in Figure 10 allows to select HydroSAR data products by country, date range, or user defined bounding box. Once a request was made, data are bundled in zip files and a download link is sent to interested users via email.

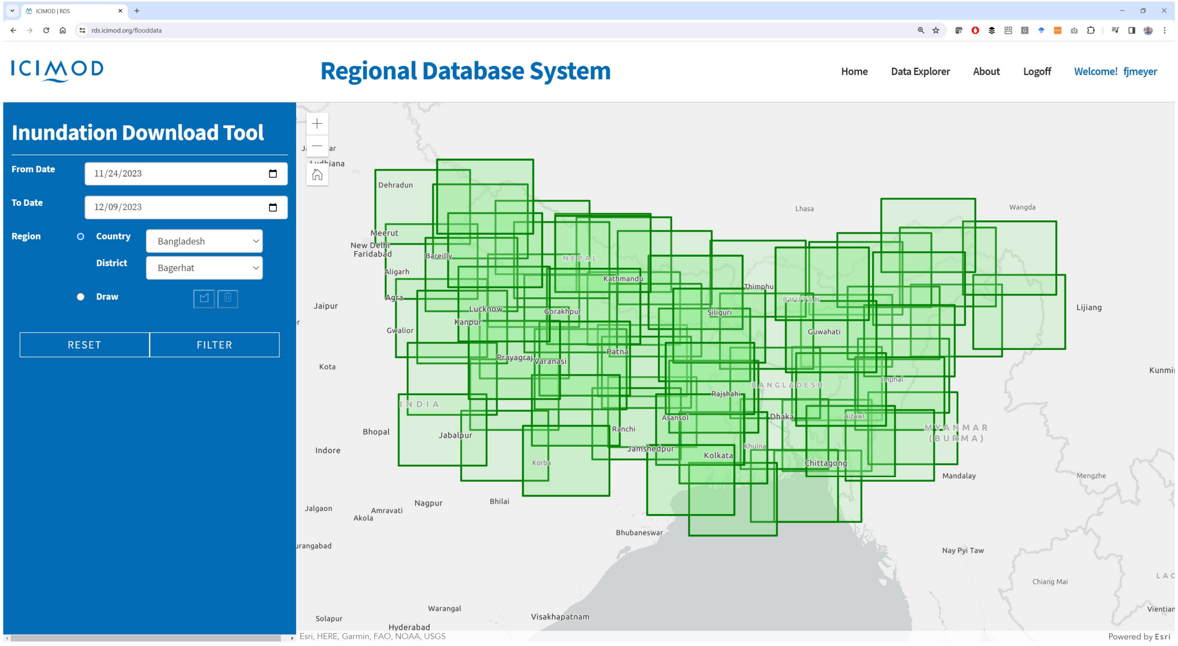

Inundation Download Tool

From Date 11/24/2023

To Date 12/09/2023

Region ○ Country Bangladesh

District Bagerhat

● Draw

RESET FILTER

Figure 10. The HydroSAR inundation data download Tool under the RDS Portal. Data can be selected by country, date range, and user-drawn AOI.

7. Validation of Quantitative HydroSAR Information Layers

Our strategy of evaluating the performance of HydroSAR data products includes two different approaches. For HYDRO30, we derived formal performance metrics by comparing HydroSAR products to estimates derived from other sensors or other approaches. For WD30, we evaluated our products by comparing them to water depth field observations available in the region.

7.1. Validating HYDRO30

We used two quantitative approaches to evaluate the performance of HYDRO30 products including (i) a comparison of HYDRO30 with water extent information extracted from multispectral imagery, and (ii) a cross-validation with water extents from a Google-developed flood forecasting model [40].

For comparisons to multispectral data, we select near-simultaneous observations of Sentinel-1 SAR and (cloud-free) Sentinel-2 or Landsat-8 images over flood-affected regions. We select these two multispectral sensors as reference as they are of similar resolution to Sentinel-1 and as established methods for detecting surface water from their data exist.

Due to persistent cloud coverage over the HKH region during the monsoon season, we could not perform comparisons to multispectral data over the HKH. Instead, we validate HYDRO30 against multispectral data for an area along the Missouri river, at the corner of Nebraska, Kansas, and Missouri, U.S.A (Figure 11). We focused on data from 2019 for this analysis, as the midwestern US experienced a major flooding event in 2019 that was fueled by heavy rainfall and melting snow [41]. This flooding event was the longest-lasting flood since 1927 in the region, giving opportunity to study HYDRO30 performance as the flood progressed.

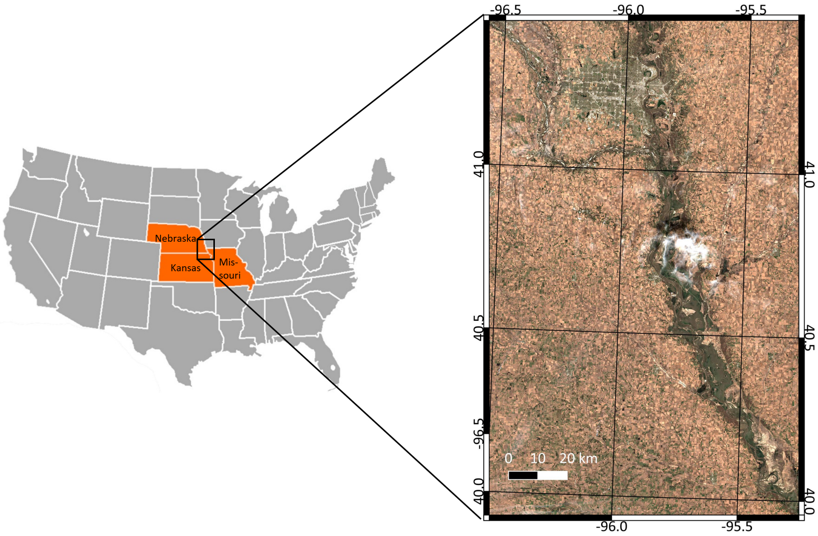

Figure 11. Validation area used to compare HYDRO30 water extent products to water extent maps derived from Landsat-8 and Sentinel-2. The site includes the Missouri river at the corner of Nebraska, Kansas, and Missouri, U.S.A.

A total of 17 date pairs of microwave (SAR) and optical (Landsat-8 and Sentinel-2) images were selected for cross-validation, with the dates falling between April and October of 2019. These data pairs were selected based on a few factors. Firstly, we required that the SAR and optical images were acquired within a 5-day window of each other. This ensures that both datasets measure comparable surface water extents. Secondly, we required that the optical images contain less than 20% cloud cover in order to reduce discrepancies based on cloud cover and cloud shadow.

We derived Water extent from Sentinel-1 using the HYDRO30 algorithm and from multispectral data using the established modified normalized difference water index (mNDWI) [42] approach. We compared the water extent information from both sensor types and calculated skill scores to evaluate HYDRO30 products. Our skill scores included accuracy ($A = {}^{((TP+TN))}/_{T}$) and precision ($P = {}^{TP}/_{(TP+FP)}$), with TP= true positives, TN= true negatives, FP= false positives, FN= false negatives, and T= total population.

An example of this approach is shown in Figure 12. There, Hydro30 water extent information is shown in the left panel while water extent mapped from optical data using nNDWI is shown in the center. The right panel is a comparison of the produced water extent information with blue areas indicating agreement, red regions indicate missed detections by HYDO30 and light blue areas indicate water detections in HYDO30 that were not present in the optical data. The example in Figure 12 demonstrates that HYDRO30 matches optical reference data with typically high accuracy (here: $A = 98\%$ and $P = 86\%$). Additional examples of Sentinel-1 (S1) and optical image comparisons are presented in Table 1, showing overall consistent water mapping skills. Throughout the 17 data pairs in our analysis, we saw an average accuracy of $A = 99\%$ and average precision of $P = 79\%$).

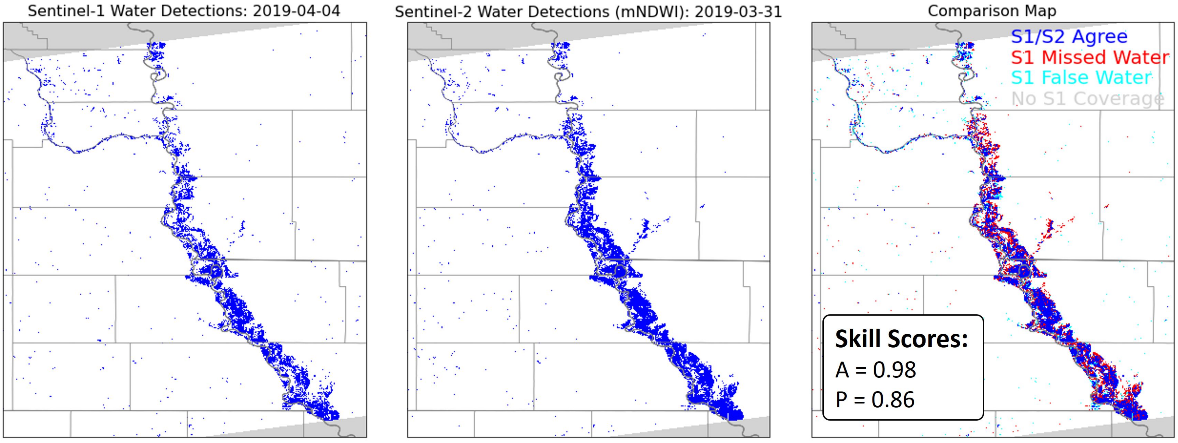

Figure 12. Comparison of HYDRO30 surface water detections to information derived from Sentinel-2 data using mNDWI. Data acquired over the Missouri river in Nebraska (Sentinel-2 on 04/04/19; Sentinel-1 on 03/31/19).

As cloud cover limits the usability of multispectral images during most of the HKH monsoon season, we augment our qualitative analysis along the Missouri river with a qualitative comparison to Google-provided flood forecasts that are available for some parts of the HKH region. Figure 13a shows a comparison of HYDRO30 data (blue) to Google flood forecasts (hash pattern) for the Kameng River, India. Both, SAR and forecast data stem from Jun-26, 2021. Figure 13b shows a similar comparison for the Brahmaputra River, Bangladesh, with SAR data from Sep-13, 2022 and forecasting information from Sep-12,2022. Good correspondence for the SAR-observed and forecasted water extents can be observed with both data sources indicating similar areas to be water covered. Note that the forecast products only captures riverine flooding and does not include the standing water bodies seen in HYDRO30 at locations away from the river.

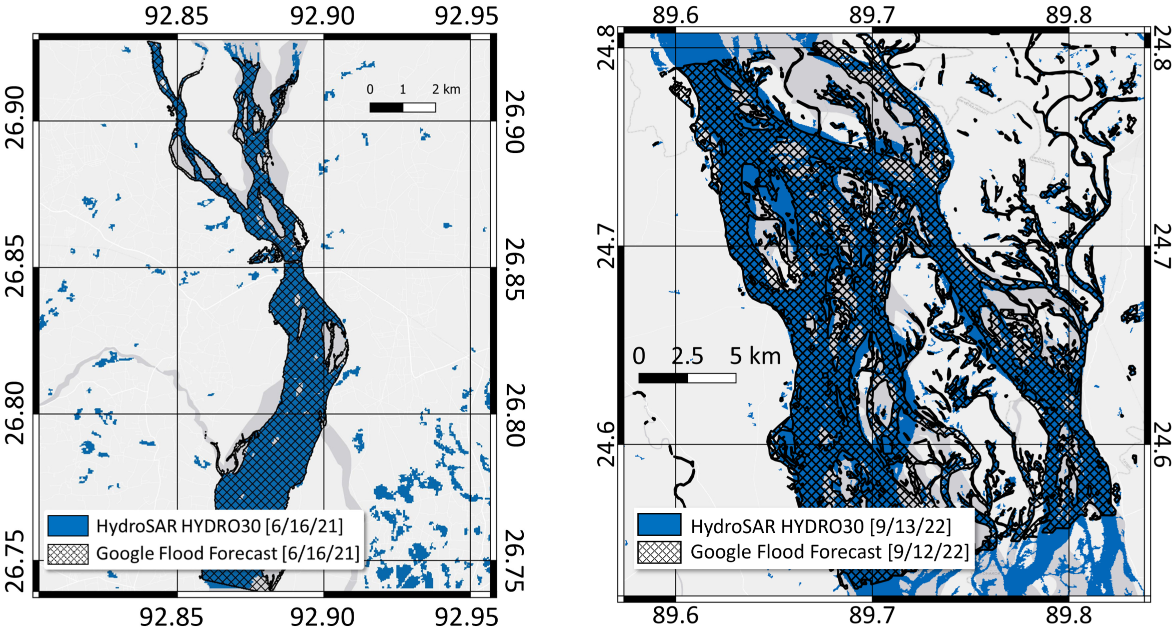

(a) (b)

Figure 13. Examples of qualitative comparisons of HYDRO30 water extent products (blue) with Google-provided flood forecasts (hash pattern): (a) Kameng River, India. SAR and forecast data from Jun-26, 2021; (b) Brahmaputra River, Bangladesh. SAR from Sep-13, 2022 and forecast from Sep-12, 2022.

Table 1. Performance metrics for pairs of SAR (S1) and optically-derived (S2) surface water extent estimates. SAR estimates derived using HyDRO30 algorithm. Optical estimate derived using mNDWI.

Skill Score	S1: 04/04 S2: 03/13	S1: 06/27 S2: 06/24	S1: 08/02 S2: 07/19	S1: 08/26 S2: 08/28	S1: 11/13 S2: 11/12
Accuracy	0.98	0.99	0.99	0.99	0.99
Precision	0.79	0.85	0.71	0.64	0.88

These comparisons to multispectral and forecasting data together with positive feedback from end-users in the region give us confidence in the performance and validity of the HYDRO30 product.

7.2. Validating WD30

To evaluate WD30 products, we use water level data from the Flood Forecasting and Warning Center-Bangladesh Water Development Board (BWDB) as reference (Figure 14a). The BWDB operates gauge stations across the country of Bangladesh and publishes water levels at these stations through their web interface. We retrieve gauging heights over validation areas, which use the Public Works Datum (PWD) established in India under British rule. The PWD reference height is about 1.5ft below the mean-sea-level. We correct a vertical offset between the BWDB datum and the EGM2008 datum used in the GLO-30 DEM (and therefore HAND and WD30). Then,m gauge station water heights are compared to the nearest valid FD30 pixel for cross-validation.

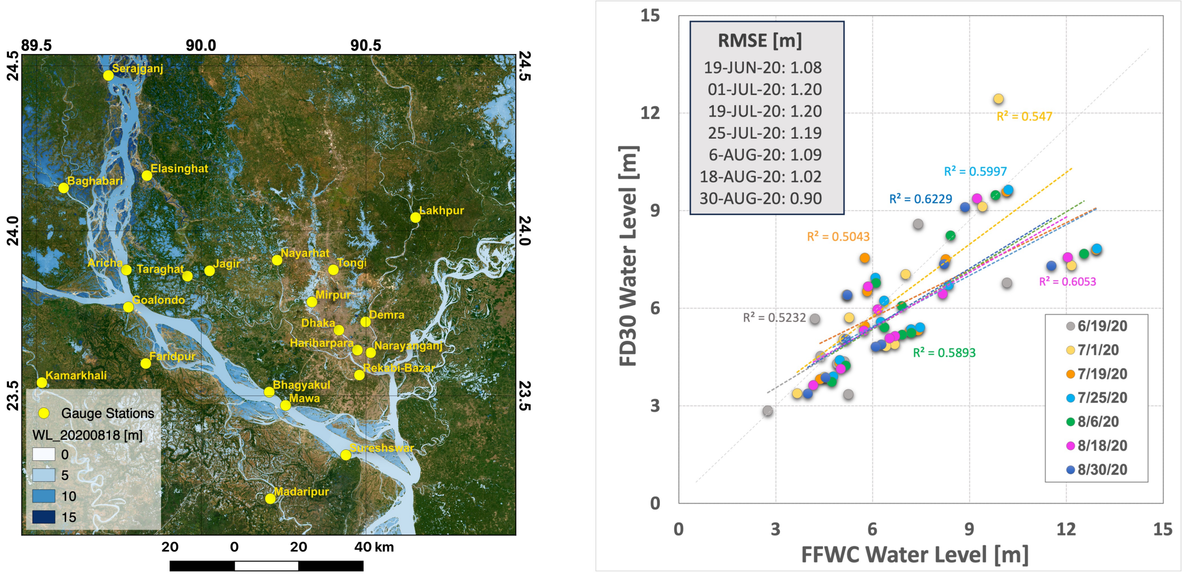

(a) (b)

Figure 14. WD30 Performance Assessments: (a) An example of SAR-derived water level map and the water level gauge stations in Bangladesh; (b) Comparison of WD30 to water level information from BWDB for the confluence of Padma and Meghna rivers, Bangladesh. Difference colors correspond to different observation dates.

Figure 14b shows a comparison of BWDB and WD30 data for the confluence of the Padma and Meghna rivers, Bangladesh. Several dates of the 2020 monsoon season are shown. R^2 values are close to 0.6 for different dates in 2020. This is because one gauge station, located in an isolated water basin, showed an exceptional range of water levels. By excluding that gauge station, R^2 near or larger than 0.8 can be observed. Also, a root mean square error (RMSE) of less than 2m was achieved for each of the analyzed dates. This is in line with the relative vertical accuracy of the Copernicus GLO-30 DEM, which is expected to be better than 2m in flat terrain (slope $< 20\%$) and better than 4m in sloping terrain (slope $> 20\%$) [43].

8. Application Example: 2023 Bangladesh Flooding Season

8.1. Background and Data

Bangladesh is a land of many rivers and as such the most flood-susceptible country in the HKH. Sitting at the confluence of three major rivers, the Ganges, Brahmaputra, and Meghna, and their tributaries [44], Bangladesh faces a number of flood-related risks such as fluvial flooding due to the accumulation of water from upstream catchments, pluvial flooding due to heavy monsoon rainfalls, and locally heavy rainfall enhanced by drainage congestion.

Bangladesh's meteorological year can be divided into three seasons, including the pre-monsoon hot season from March to May, the rainy monsoon season lasting from June through October, and a cool, dry winter season from November through February. The country has an average of 136 wet days per year, and approximately 80% of yearly rainfall occurs from June to September [4]. Most flooding occurs during the monsoon season, covering up to 31,000 square kilometers or around 21% of the country in water. During the most severe flood seasons, up to two-thirds of the country can be covered in water, as was seen during the 1998 monsoon [45].

Here we analyze the progression of the 2023 monsoon season for the country of Bangladesh (Figure 15) using operationally-generated HydroSAR HYDRO30 data products. The 2023 season was chosen as it was the most recently monitored monsoon season at the time of writing of this article. Furthermore, the 2023 season was impacted by cyclonic storm Mocha, a powerful and deadly tropical cyclone that made landfall in southern Bangladesh on May 14, 2023. We evaluate flood extent and flood impacts across the country of Bangladesh and as a function of time. All data used in this analysis were retrieved through the ICIMOD RDS services introduced in Section 6.

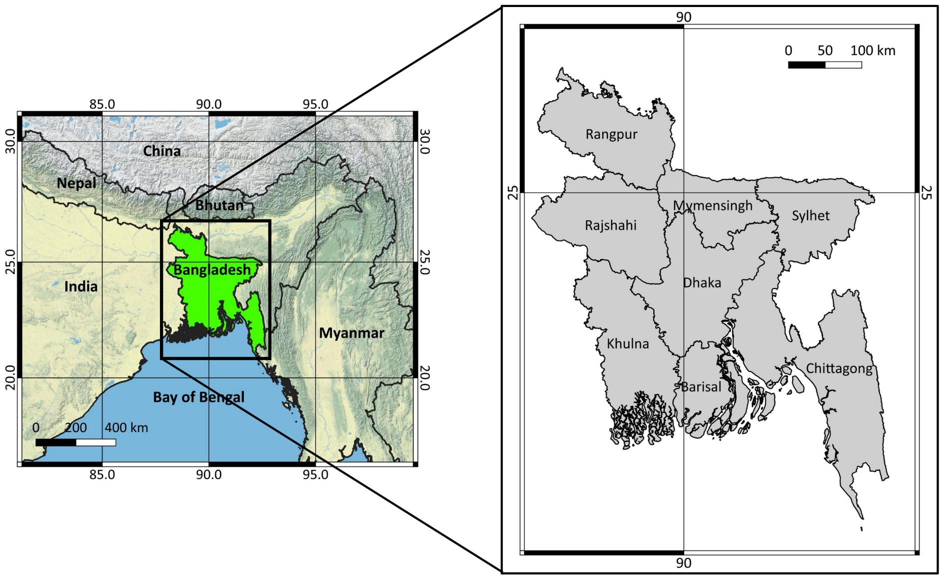

Figure 15. Left: Area of Interest (AOI) for countrywide analysis of surface water extent for the flood year 2023. Right: Map of Bangladesh administrative divisions. These divisions are further analyzed in Section 8.2.

A total of 719 Sentinel-1 SAR-derived HYDRO30 products were collected to derive full-coverage surface water extent information in 2-week/14-days intervals starting on January 1st and ending on December 31st of 2023. A total of 25 14-day flood area maps were compiled from these data. The 14-days integration period was chosen to ensure full wall-to-wall coverage of the Bangladesh by Sentinel-1 SAR data. Each 14-day map combines information from an average of 29 individual scenes.

8.2. 2023 Bangladesh Flood Progression

Figure 16 shows the results of a time-series analysis of surface water extent throughout the 2023 Bangladesh flood season as derived from all available HYDRO30 data. The results show that surface water extent slowly decreased early in the year as residual water from the previous monsoon season dried up during the dry post-monsoon winter season. A minimum surface water extent of 6,549.5km^2 or 4.42% of the Bangladesh land area was reached on April 02, 2023, near the end of the dry pre-monsoon season. We interpret this extent as the perennial water extent in Bangladesh.

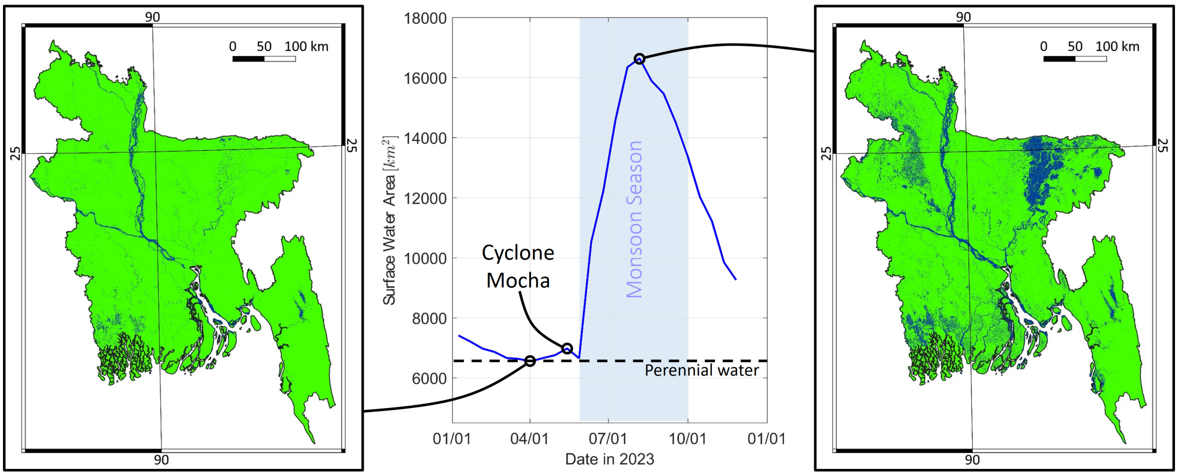

Figure 16. Time series of surface water extent in Bangladesh throughout 2023 as derived from HYDRO30 products. Left: minimum water extent occurring on April 02, 2023; middle: Surface water extent time series; right: Maximum Water extent on August 06, 2023.

A small uptick in water extent can be observed for the time step centered on May 14, 2023. This peak is coincident with the landfall of cyclone Mocha that caused increased water coverage in Bangladesh's southern divisions Khulna (southwest) and Chittagong (souteast).

A rapid increase of water extent commenced around May 28th, marking the onset of the monsoon season. The maximum water extent of 17,138.4km^2 or 11.6% of land area was reached around Aug 6, 2023, marking 2023 as a below-average monsoon season for Bangladesh. After Aug 6, surface water started slowly and progressively receding through the rest of the year.

Bangladesh is divided into eight administrative divisions (Figure 15) that are differently affected by monsoon-related flooding. A division-by-division assessment of surface water extent (Figure 17) shows that a vast majority of the inundation occurred in the northeastern Sylhet Division of Bangladesh. Sylhet is a low-lying area that often acts as a natural "reservoir" for monsoon-related floodwaters. At the peak of the 2023 monsoon season, 31.1% of Sylhet was covered in water. The Chittagong Division, located in the southeast of Bangladesh, showed the least surface water area relative to its area (6.7%). This is due to the lack of major rivers draining into this division and due to its higher average topography.

The available data also allows to determine the timing of peak water extent for each division (see text in Figure 17). Our data show that the peak flooding dates were reasonably consistent across Bangladesh with flood waters peaking around Aug 6, 2023 in most divisions. Maximum water extent occurred slightly earlier in the Sylhet and Khulna divisions (Jul 23, 2023) and slightly later in Barisal (Sep 3, 2023).

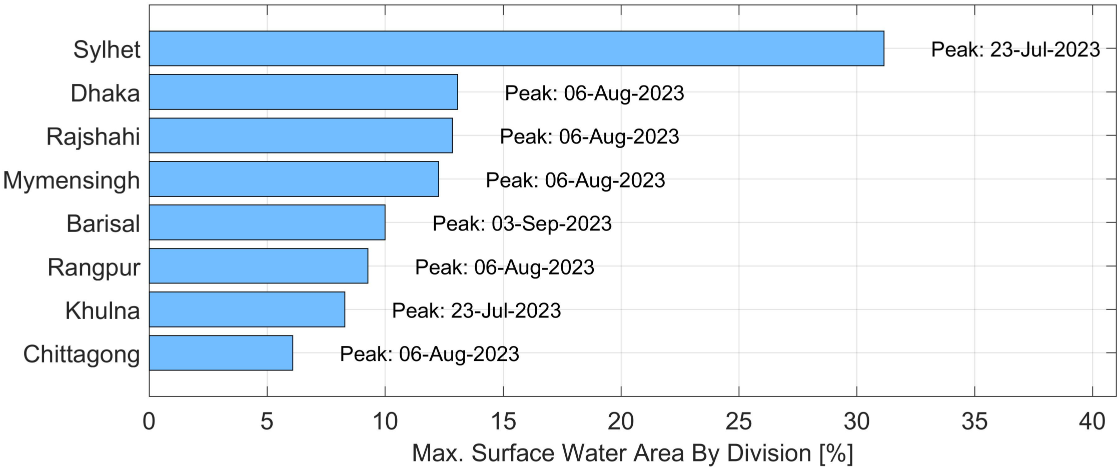

Figure 17. Maximum surface water extent for different divisions of Bangladesh in percent of overall division area as calculated from HydroSAR HYDRO30 mosaics.

8.3. Total Annual Flood Duration Analysis

How long a particular patch of land was inundated is a relevant metric to assess the impact of flooding on agricultural crop yields, building integrity, transportation infrastructure, and other landscape functions. Furthermore, it can help in the assessment of the evolution of an inundation event and can be used to support disaster mitigation and prevention by indicating areas most severely affected by floods [15].

We estimate the *total annual flood duration (TAFD)* from our 2023 HydroSAR HYDRO30 data time series following an approach published in [15]. According to this approach, TAFD is computed per pixel using all data generated within a calendar year. To provide an accurate count of inundation days, we allow for the possibility that a pixel is covered by more than one flood event, accounting for flood-free periods in between. Therefore, similar to [15], we first calculate the duration of each of the n ($n \leq 1$) inundation events separately and then sum all n event durations to arrive at the total flood duration in days.

$$TAFD_i = \sum_{i=1}^{n} D_{d,i} - D_{c,i} \tag{4}$$

where $D_{c,i}$ is the first and $D_{d,i}$ is the last day inundation was observed for event i.

Figure 18a shows the results of this analysis for the 2023 flood season. For ease of visualization, the TAFD results are categorized into four categories: White pixels were never inundated; green areas were inundated for less than 30 days; red areas were inundated for $30 \leq$ days < 100; and blue pixels were water covered for $100 \leq$ days < 200.

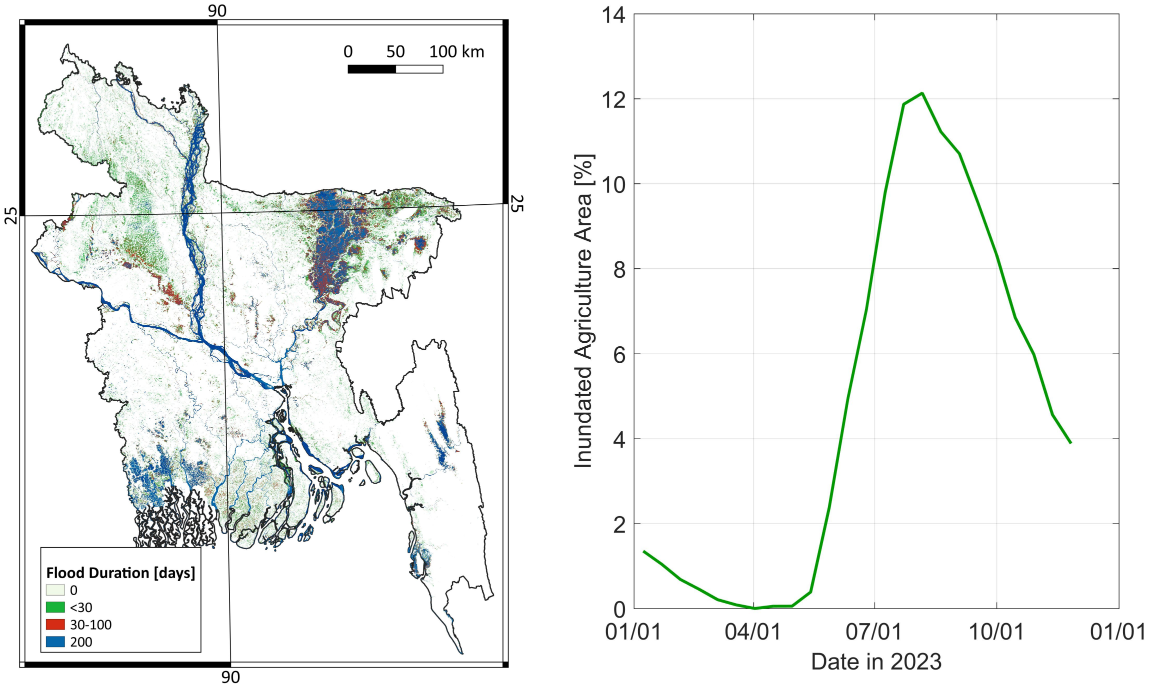

(a) **(b)**

Figure 18. Total annual flood duration and flood impacted agriculture areas: (a) Total annual flood duration (TAFD) per pixel as calculated from HYDRO30 time series. Data are categorized into four classes as shown in the legend; (b) extent of flood-impacted agriculture areas as a function of time, calculated by intersecting HYDRO30 information with agriculture extent information extracted from the Copernicus Global Land Monitoring Service.

It can be seen that large areas of the low-lying Sylhet Division in northeastern Bangladesh were water covered for more than 100 days. Long-lasting inundation can also be observed for some areas of the southwestern Khulna Division. Note that permanent water are included in this category.

Areas affected by short duration (less than 30 days) flooding can be found throughout the country, but occur most prominently in the Rajshahi and Rangpur divisions as well as in the Mymensingh, Barisal, and Sylhet divisions.

8.4. Affected Agriculture Areas

As HydroSAR's AG30 agriculture extent product is not yet fully operationally implemented, we used the Dynamic Land Cover Product version 3, distributed by the Copernicus Global Land Monitoring Service [27], to assess the impact of the 2023 flood season on Bangladesh's agriculture regions. This 100m-resolution product offers annual global land cover information derived from observations of the PROBA-V satellite [46]. The latest version of this product was assessed to achieve a classification accuracy of 80% on each continent [27]. We extract agriculture extent information from this product and resample the extracted layer to match the posting of the HYDRO30 products for further joint analysis.

We first derive the time series of agriculture inundation by intersecting the agriculture extent layer with the bi-weekly HYDRO30 surface water extent information. The results of this analysis are shown in Figure 18b. Similar to the water extent time series in Figure 16, we observe minimum inundated agriculture in early April. Agriculture inundation started to increase with the onset of the monsoon and reached a maximum on Aug 6, 2023, where 13.5% of all agriculture lands were identified as water covered. Inundation dropped rapidly after this date as monsoon waters began to recede.

In flood situations, the extent of crop damage and therefore the impact on crop yield often depends on the duration of flooding. To study how long Bangladesh's flood-affected agriculture lands were inundated, we can intersect Copernicus agriculture extent information with the TAFD layer shown in Figure 18a. Note that this analysis will reveal how long a certain agriculture patch was inundated but does not allow to assess when this inundation occurred.

Figure 19 shows that 11.2% of Bangladesh's agriculture areas were inundated for 30 days or less, while 5.3% or crop lands were inundated between 30 and 100 days, and 4.6% of Bangladesh's agriculture areas were inundated for more than 100 days. Combined with information about crop type, this data could help in the evaluation of flood impacts on food production.

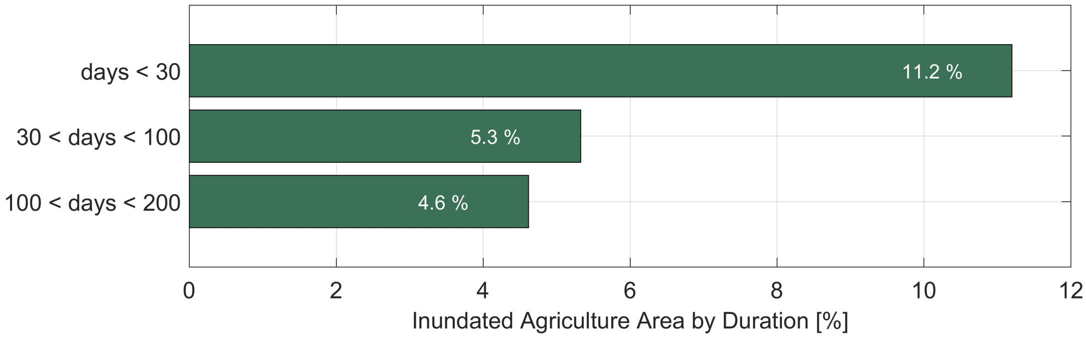

Figure 19. Agriculture areas covered in water as a function of flooding duration, calculated by intersecting AG with TAFD.

The examples shown in Section 8 provide some indication of the value of the HydroSAR service for flood analysis in the region. Beyond the retrospective studies shown here, HydroSAR data can serve a range of other applications such as the analysis of individual flooding events or the statistical analysis of multiple years of data in support of flood mitigation.

9. Summary and Conclusions

We collaborated closely with partners in the HKH to develop HydroSAR, a SAR data processing and analysis service focused on the automatic, year-round, and near real-time generation of flood information products for this region. To meet end-user needs, HydroSAR was designed with a broad product suite in mind that enables the simultaneous assessment of several flood-related parameters as events unfold and progress. The service uses Sentinel-1 SAR data as input and is fully cloud-based to enable rapid product generation at scale. A tight integration with ASF's cloud-based Sentinel-1 SAR archives ensures that data do not have to be migrated out of the cloud, maximizing throughput and minimizing processing costs.

The service was successfully transitioned to ICIMOD, a regional organization in the HKH, who continue to operate HydroSAR and provide its data to end-users through a dedicated web portal. An application of HydroSAR to analyze the 2023 southeast Asia monsoon season showcases one of many potential use cases of HydroSAR, and demonstrates the amount of information that can be extracted from the available data.

The team continues to improve the service in collaboration with its partners. We are preparing for the integration of data from the highly anticipated NASA-ISRO SAR (NISAR) mission, currently scheduled for launch in 2024. We are also investigating machine learning algorithms that would combine SAR data with river discharge forecasts to enable daily flood water extent forecasting.

Author Contributions: Conceptualization, F.J.M., R.B.T.; methodology, F.J.M., B.O., M.J., J.H.K., and L.A.S.; software, F.J.M., B.O., M.J., J.H.K., and J.S.; validation, F.J.M., M.J. and L.A.S.; formal analysis, F.J.M. and B.O.; investigation, F.J.M.; resources, F.J.M.; data curation, J.H.K. and S.P; writing—original draft preparation, F.J.M.; writing—review and editing, B.O., M.J., R.B.T., J.H.K., and L.A.S.; visualization, F.J.M., M.J. and R.B.T.; supervision,

F.J.M., B.O., and L.A.S.; project administration, F.J.M.; funding acquisition, F.J.M. All authors have read and agreed to the published version of the manuscript.

Funding: This research was funded by NASA Science Mission Directorate under grant numbers #80NSSC20K0164 & #80NSSC19K1109.

Data Availability Statement: All data presented in this report are openly accessible through the ICIMOD Flood Inundation portal at https://geoapps.icimod.org/Floodinundation/ and can be downloaded through the ICIMOD Regional Database System (RDS). The software implementations of all HydroSAR algorithms are available on an open GitHub repository at https://github.com/HydroSAR/HydroSAR.

Acknowledgments: Products provided by the HydroSAR service are derived from Copernicus Sentinel data, processed by ESA. Sentinel-1 data are accessed to the services of the NASA Alaska Satellite Facility (ASF) Distributed Active Archive Center (DAAC).

We thank the ASF HyP3 team for their support of the cloud implementation of our workflows. We owe gratitude to the team at the NASA SERVIR Science Coordination Office for their support and guidance. We thank our partners at ICIMOD and their connected end users for their input and collaboration.

Conflicts of Interest: The authors declare no conflicts of interest.

References

1. Vaidya, R.A.; Shrestha, M.S.; Nasab, N.; Gurung, D.R.; Kozo, N.; Pradhan, N.S.; Wasson, R.J. Disaster risk reduction and building resilience in the Hindu Kush Himalaya. *The Hindu Kush Himalaya assessment: Mountains, climate change, sustainability and people* **2019**, pp. 389–419.
2. Bajracharya, B.; Thapa, R.B.; Matin, M.A. *Earth Observation Science and Applications for Risk Reduction and Enhanced Resilience in Hindu Kush Himalaya Region: A Decade of Experience from SERVIR*; Springer Nature, 2021.
3. Shrestha, M.S.; Grabs, W.E.; Khadgi, V.R. Establishment of a regional flood information system in the Hindu Kush Himalayas: challenges and opportunities. *International Journal of Water Resources Development* **2015**, *31*, 238–252.
4. Uddin, K.; Matin, M.A.; Meyer, F.J. Operational flood mapping using multi-temporal Sentinel-1 SAR images: A case study from Bangladesh. *Remote Sensing* **2019**, *11*, 1581.
5. Potin, P.; Bargellini, P.; Laur, H.; Rosich, B.; Schmuck, S. Sentinel-1 mission operations concept. In Proceedings of the 2012 IEEE international geoscience and remote sensing symposium. IEEE, 2012, pp. 1745–1748.
6. Kellogg, K.; Hoffman, P.; Standley, S.; Shaffer, S.; Rosen, P.; Edelstein, W.; Dunn, C.; Baker, C.; Barela, P.; Shen, Y.; et al. NASA-ISRO synthetic aperture radar (NISAR) mission. In Proceedings of the 2020 IEEE Aerospace Conference. IEEE, 2020, pp. 1–21.
7. Martinis, S.; Twele, A.; Voigt, S. Towards operational near real-time flood detection using a split-based automatic thresholding procedure on high resolution TerraSAR-X data. *Natural Hazards and Earth System Sciences* **2009**, *9*, 303–314.
8. Long, S.; Fatoyinbo, T.E.; Policelli, F. Flood extent mapping for Namibia using change detection and thresholding with SAR. *Environmental Research Letters* **2014**, *9*, 035002.
9. Seitz, F.; Hedman, K.; Meyer, F.J.; Lee, H. Multi-sensor space observation of heavy flood and drought conditions in the Amazon region. In Proceedings of the Earth on the Edge: Science for a Sustainable Planet: Proceedings of the IAG General Assembly, Melbourne, Australia, June 28-July 2, 2011. Springer, 2014, pp. 311–317.
10. Meyer, F.; McAlpin, D.; Gong, W.; Ajadi, O.; Arko, S.; Webley, P.; Dehn, J. Integrating SAR and derived products into operational volcano monitoring and decision support systems. *ISPRS journal of photogrammetry and remote sensing* **2015**, *100*, 106–117.
11. Ajadi, O.A.; Meyer, F.J.; Webley, P.W. Change detection in synthetic aperture radar images using a multiscale-driven approach. *Remote Sensing* **2016**, *8*, 482.
12. Twele, A.; Cao, W.; Plank, S.; Martinis, S. Sentinel-1-based flood mapping: a fully automated processing chain. *International Journal of Remote Sensing* **2016**, *37*, 2990–3004.
13. Tran, K.H.; Menenti, M.; Jia, L. Surface water mapping and flood monitoring in the Mekong Delta using sentinel-1 SAR time series and Otsu threshold. *Remote Sensing* **2022**, *14*, 5721.

14. Qiu, J.; Cao, B.; Park, E.; Yang, X.; Zhang, W.; Tarolli, P. Flood monitoring in rural areas of the Pearl River Basin (China) using Sentinel-1 SAR. *Remote Sensing* **2021**, *13*, 1384.
15. Martinis, S.; Wieland, M.; Rättich, M. An Automatic System for Near-Real Time Flood Extent and Duration Mapping Based on Multi-Sensor Satellite Data. In *Earth Observation for Flood Applications*; Elsevier, 2021; pp. 7–37.
16. Ozaki, M. Disaster risk financing in Bangladesh. *Working Paper Series* **2016**.
17. Hussain, A.; Rasul, G.; Mahapatra, B.; Tuladhar, S. Household food security in the face of climate change in the Hindu-Kush Himalayan region. *Food Security* **2016**, *8*, 921–937.
18. Manjusree, P.; Prasanna Kumar, L.; Bhatt, C.M.; Rao, G.S.; Bhanumurthy, V. Optimization of threshold ranges for rapid flood inundation mapping by evaluating backscatter profiles of high incidence angle SAR images. *International Journal of Disaster Risk Science* **2012**, *3*, 113–122.
19. Thapa, R.B.; Bajracharya, B.; Matin, M.A.; Anderson, E.; Epanchin, P. Service planning approach and its application. *A Decade of Experience from SERVIR* **2021**, p. 23.
20. Molden, D.; Sharma, E. ICIMOD's strategy for delivering high-quality research and achieving impact for sustainable mountain development. *Mountain Research and Development* **2013**, *33*, 179–183.
21. Cigna, F.; Xie, H. Imaging floods and glacier geohazards with remote sensing, 2020.
22. Bell, J.; Kubby, B.; Meyer, F.; Yadav, S. Identifying and Mapping Agricultural Areas Using Synthetic Aperture Radar Time Series. In Proceedings of the AGU Fall Meeting Abstracts, 2021, Vol. 2021, pp. GC45I–0925.
23. Copernicus DEM, 2022. https://doi.org/10.5270/esa-c5d3d65.
24. Zink, M.; Moreira, A.; Hajnsek, I.; Rizzoli, P.; Bachmann, M.; Kahle, R.; Fritz, T.; Huber, M.; Krieger, G.; Lachaise, M.; et al. TanDEM-X: 10 years of formation flying bistatic SAR interferometry. *IEEE Journal of Selected Topics in Applied Earth Observations and Remote Sensing* **2021**, *14*, 3546–3565.
25. Wessel, B.; Huber, M.; Wohlfart, C.; Marschalk, U.; Kosmann, D.; Roth, A. Accuracy assessment of the global TanDEM-X Digital Elevation Model with GPS data. *ISPRS Journal of Photogrammetry and Remote Sensing* **2018**, *139*, 171–182.
26. Lehner, B.; Verdin, K.; Jarvis, A. New global hydrography derived from spaceborne elevation data. *Eos, Transactions American Geophysical Union* **2008**, *89*, 93–94.
27. Buchhorn, M.; Lesiv, M.; Tsendbazar, N.E.; Herold, M.; Bertels, L.; Smets, B. Copernicus global land cover layers—collection 2. *Remote Sensing* **2020**, *12*, 1044.
28. Nobre, A.D.; Cuartas, L.A.; Hodnett, M.; Rennó, C.D.; Rodrigues, G.; Silveira, A.; Saleska, S. Height Above the Nearest Drainage–a hydrologically relevant new terrain model. *Journal of Hydrology* **2011**, *404*, 13–29.
29. Hogenson, K.; Kristenson, H.; Kennedy, J.; Johnston, A.; Rine, J.; Logan, T.; Zhu, J.; Williams, F.; Herrmann, J.; Smale, J.; et al. Hybrid Pluggable Processing Pipeline (HyP3): A cloud-native infrastructure for generic processing of SAR data, 2024. https://doi.org/10.5281/zenodo.10854802.
30. Small, D.; Zuberbühler, L.; Schubert, A.; Meier, E. Terrain-flattened gamma nought Radarsat-2 backscatter. *Canadian Journal of Remote Sensing* **2011**, *37*, 493–499.
31. Shiroma, G.H.; Lavalle, M.; Buckley, S.M. An area-based projection algorithm for SAR radiometric terrain correction and geocoding. *IEEE Transactions on Geoscience and Remote Sensing* **2022**, *60*, 1–23.
32. Small, D. Flattening gamma: Radiometric terrain correction for SAR imagery. *IEEE Transactions on Geoscience and Remote Sensing* **2011**, *49*, 3081–3093.
33. Frey, O.; Santoro, M.; Werner, C.L.; Wegmuller, U. DEM-based SAR pixel-area estimation for enhanced geocoding refinement and radiometric normalization. *IEEE Geoscience and Remote Sensing Letters* **2012**, *10*, 48–52.
34. Martinis, S.; Kersten, J.; Twele, A. A fully automated TerraSAR-X based flood service. *ISPRS Journal of Photogrammetry and Remote Sensing* **2015**, *104*, 203–212.
35. Meyer, F.J.; Schultz, L.; Bell, J.; Molthan, A.L.; Osmanoglu, B.; Jo, M.; Lundell, E.; Chapman, B.D.; Kubby, B.; Meyer, T.; et al. Monitoring Weather-Related Hazards Using the HydroSAR Service: Application to the 2020 South Asia Monsoon Season. In Proceedings of the 2021 IEEE International Geoscience and Remote Sensing Symposium IGARSS. IEEE, 2021, pp. 893–896.
36. Pekel, J.F.; Cottam, A.; Gorelick, N.; Belward, A.S. High-resolution mapping of global surface water and its long-term changes. *Nature* **2016**, *540*, 418–422.
37. Olson, B.; Shehu, A. Efficient basin hopping in the protein energy surface. In Proceedings of the 2012 IEEE International Conference on Bioinformatics and Biomedicine. IEEE, 2012, pp. 1–6.

38. Hogenson, K.; Arko, S.A.; Buechler, B.; Hogenson, R.; Herrmann, J.; Geiger, A. Hybrid Pluggable Processing Pipeline (HyP3): A cloud-based infrastructure for generic processing of SAR data. In Proceedings of the Agu fall meeting abstracts, 2016, Vol. 2016, pp. IN21B–1740.
39. Rad, B.B.; Bhatti, H.J.; Ahmadi, M. An introduction to docker and analysis of its performance. *International Journal of Computer Science and Network Security (IJCSNS)* **2017**, *17*, 228.
40. Nevo, S.; Morin, E.; Gerzi Rosenthal, A.; Metzger, A.; Barshai, C.; Weitzner, D.; Voloshin, D.; Kratzert, F.; Elidan, G.; Dror, G.; et al. Flood forecasting with machine learning models in an operational framework. *Hydrology and Earth System Sciences* **2022**, *26*, 4013–4032.
41. Pal, S.; Lee, T.R.; Clark, N.E. The 2019 Mississippi and Missouri River flooding and its impact on atmospheric boundary layer dynamics. *Geophysical Research Letters* **2020**, *47*, e2019GL086933.
42. Xu, H. Modification of normalised difference water index (NDWI) to enhance open water features in remotely sensed imagery. *International journal of remote sensing* **2006**, *27*, 3025–3033.
43. Fahrland, E.; Jacob, P.; Schrader, H.; Kahabka, H. Copernicus digital elevation model—Product handbook. *Airbus Defence and Space—Intelligence: Potsdam, Germany* **2020**.
44. Haque, M.N.; Siddika, S.; Sresto, M.A.; Saroar, M.M.; Shabab, K.R. Geo-spatial analysis for flash flood susceptibility mapping in the North-East Haor (Wetland) Region in Bangladesh. *Earth Systems and Environment* **2021**, *5*, 365–384.
45. AM, D.; Nishigaki, M.; Komatsu, M. Floods in Bangladesh: A comparative hydrological investigation on two catastrophic events. **2003**, *8*, 53–62.
46. Francois, M.; Santandrea, S.; Mellab, K.; Vrancken, D.; Versluys, J. The PROBA-V mission: The space segment. *International Journal of Remote Sensing* **2014**, *35*, 2548–2564.